XXIV Biennial Symposium on Measuring Techniques in Turbomachinery
Prague, Czech Republic, 29 - 31 August 2018
Paper No MTT2418A43

THE DECOUPLING PROBLEM: SEPARATING UNDERLYING BOUNDARY CONDITIONS IN METAL EFFECTIVENESS MEASUREMENTS

M. Michaud, T. Povey
Osney Thermofluids Laboratory, University of Oxford
UK

Keywords: cooling effectiveness, boundary conditions, decoupling techniques

ABSTRACT

Overall cooling effectiveness measurements (or metal effectiveness measurements) are becoming increasingly used to understand complex coupled systems in gas turbine experimental research. Unlike traditional techniques in which individual boundary conditions are measured in isolation and superposed using a thermal model, overall cooling effectiveness measurements give the final result of a complex coupled system. In correctly scaled experiments this allows aerothermal performance at near-engine conditions to be evaluated directly, and is thus powerful both as a research technique and for de-risking engine development programmes. The technique is particularly useful for evaluating the thermal performance of heavily cooled (both internal and film) nozzle guide vanes, because of the complexity and degree of interaction of the underlying boundary conditions. An intrinsic limitation of metal effectiveness measurement data is that the individual boundary conditions (the internal and external heat transfer coefficients, and film cooling effectiveness, for example) cannot be directly obtained from the final measurement. *Decoupling* of these boundary conditions would allow deeper understanding of the systems which are the subject of experiments.

The objective of this paper is to present methods to extract the individual underlying boundary conditions from data available in typical overall cooling effectiveness experimental measurements, and to assess the uncertainty associated with decoupling techniques. Although we reference experimental data from advanced facilities for metal effectiveness research throughout, much of the analysis is performed using a low-order heat transfer model to allow the impact of experiment design and measurement errors to be clearly separated at each stage of the analysis.

NOMENCLATURE

Roman variables

b	thickness, m
c	specific heat capacity, J kg^{-1} K^{-1}
h	heat transfer coefficient, W m^{-2} K^{-1}
k	thermal conductivity, W m^{-1} K^{-1}
t	time, s
T	temperature, K
y	position through the wall, m

Greek variables

α	thermal diffusivity, m^2 s^{-1}
β	bias error, K
δ	fraction
Δ	difference
ε	precision error, K
μ	mean
ϕ	normalised temperature
σ	standard deviation
ρ	density, kg m^{-3}
τ	time constant, s

Subscripts

e	end
j	wall node index
meas	measured value
n	number of nodes in the wall
ptr	particular
s	start
step	temperature step change property
trg	target value
w	wall property
0	total property
1	external side
2	internal side

Superscripts

p	time step index

Abbreviations

HTC	heat transfer coefficient
IR	infrared
PDF	probability density function
Re	Reynolds number

INTRODUCTION

Research investment in overall cooling effectiveness measurement techniques has been driven by the desire to accurately assess the overall thermal performance of nozzle guide vanes or turbine blades at engine-realistic conditions [1-6].

The traditional approach of predicting overall thermal performance of such parts from a thermal model with boundary conditions obtained from separate experiments [7-10] has the disadvantage that errors in underlying measurements can accumulate in the final result. Additionally, certain coupling terms are inherently absent in the separated experiments, limiting the accuracy of the predicted performance even in the absence of experimental errors. Metal effectiveness techniques are arguably more suited to overall performance assessment than the traditional method. One limitation, however, is that underlying boundary conditions are not automatically determined from the metal effectiveness measurement. Doing so would prevent a number of advantages to both researchers and engine designers, but is not an entirely straightforward process, not least because of the relative complexity of establishing (and even describing) confidence limits on the decoupled variables. Consider, for example, that the relationship—ratios of values, for example—between a number of variables may be known with a considerably higher degree of confidence than the value of any single variable, and that this information in itself may be of considerable value in solving certain types of problem. We refer to these complexities in the most general form as *the decoupling problem*.

The paper is structured around various simplified elemental problems, designed to typify certain aspects of the overall problem in such a way that the behaviour of the system can be understood. These are:

1) *Impact of precision and bias errors in one-dimensional system to a step change in the external flow temperature*. We use this idealized system to understand the impact of precision and bias errors in measurements of external flow temperature, internal flow temperature, and external wall temperature on the accuracy with which the underlying (extracted) boundary condition values of h_1 and h_2 can be determined.

2) *Impact of time constant of the temperature step in one-dimensional system subject to a step change in external flow temperature.* We use this idealized system to understand the impact of experimental design (in terms of realistically achievable time constants) on the accuracy with which the underlying (extracted) boundary condition values of h_1 and h_2 can be determined.

3) *Practical applications.* We consider specific examples on how we can extract and use the underlying boundary conditions from a metal effectiveness experiment.

MODELLING

The tool used in this study is a transient low-order one-dimensional heat transfer model. As shown in figure 1, the model consists of a flat wall subjected to a hot external flow of temperature $T_{01}(t)$ and a heat transfer coefficient h_1 on its external surface, and an internal flow of temperature $T_{02}(t)$ and a heat transfer coefficient h_2 on its internal surface.

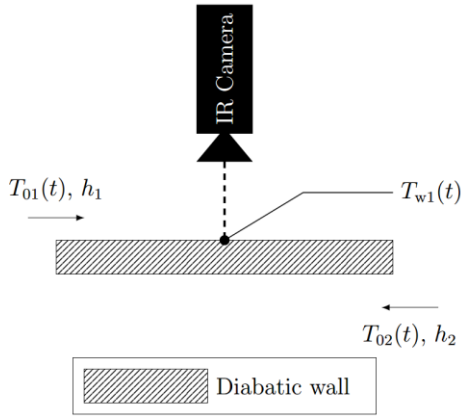

Figure 1: One-dimensional heat transfer model

$T_{01}(t)$ corresponds to an exponential temperature step change of time constant τ_{step} and amplitude ΔT_{01} (given by equation 1) and T_{02} remains constant at ambient temperature over time. The wall properties correspond to those of Inconel [11], which is a typical material for high pressure turbine parts. The properties are listed in table 1 and are fixed for the whole analysis.

$$T_{01}(t) = \Delta T_{01}(1 - e^{-t/\tau_{\text{step}}}) + T_{01}(0) \quad \#(1)$$

Table 1: Wall properties

Property	Symbol	Value
Wall conductivity	k_w	11.7 W m^{-1} K^{-1}
Wall thermal diffusivity	α_w	3.13×10^{-6} m^2 s^{-1}
Wall thickness	b_w	2.00×10^{-3} m
Wall specific heat capacity	c_w	440 J kg^{-1} K^{-1}
Wall density	ρ_w	8.28×10^3 kg m^{-3}

The transient convection at the surfaces of the wall and the conduction inside the wall are solved using finite differences to approximate the temporal and spatial derivatives of the 1D heat equation (equation 2). The solving methodology used is the one proposed by Bergman [12]. The wall is spatially discretized into n nodes as shown in figure 2 and an energy balance is applied to each node, which allows to calculate the temperature at the next time step ($T_{w,j}^{p+1}$) for any node j. Three types of nodes can be distinguished into this spatial discretization: exterior surface node ($j = 1$), interior node ($j = 2, \dots, n-1$) and internal surface

node ($j = n$), which can be solved using respectively equations 3 to 5. The simulation parameters are presented in table 2. The number of nodes (n = 41) was chosen to have a wall discretization Δy (equation 6) fine enough for the simulation's result to be independent of the discretization. The time discretization Δt corresponds to the minimum time discretization satisfying the stability conditions of each type of nodes in the spatial discretization (external surface node, interior node and internal surface node) as expressed by equation 7.

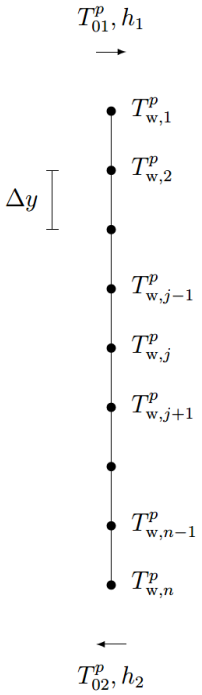

Figure 2: Discretization of the wall

$$\frac{1}{\alpha_\mathrm{w}}\frac{\partial T_\mathrm{w}}{\partial t} = \frac{\partial^2 T_\mathrm{w}}{\partial y^2} \tag{2}$$

$$T_{\mathrm{w},1}^{p+1} = \frac{2h_1\Delta t}{\rho_\mathrm{w} c_\mathrm{w}\Delta y}\left(T_{01}^p - T_{\mathrm{w},1}^p\right) + T_{\mathrm{w},1}^p + \frac{2\alpha_\mathrm{w}\Delta t}{\Delta y^2}\left(T_{\mathrm{w},2}^p - T_{\mathrm{w},1}^p\right) \tag{3}$$

$$T_{\mathrm{w},j}^{p+1} = T_{\mathrm{w},j}^p + \frac{k_\mathrm{w}\Delta t}{\rho_\mathrm{w} c_\mathrm{w}\Delta y^2}\left(T_{\mathrm{w},j-1}^p + T_{\mathrm{w},j+1}^p - 2T_{\mathrm{w},j}^p\right) \tag{4}$$

$$T_{\mathrm{w},n}^{p+1} = \frac{2h_2\Delta t}{\rho_\mathrm{w} c_\mathrm{w}\Delta y}\left(T_{02}^p - T_{\mathrm{w},n}^p\right) + T_{\mathrm{w},n}^p + \frac{2\alpha_\mathrm{w}\Delta t}{\Delta y^2}\left(T_{\mathrm{w},n-1}^p - T_{\mathrm{w},n}^p\right) \tag{5}$$

$$\Delta y = b_\mathrm{w}/(n-1) \tag{6}$$

$$\Delta t = \min\left\{\frac{k_\mathrm{w}(\Delta y)^2}{2\alpha_\mathrm{w}(1+h_1\Delta y)}, \frac{(\Delta y)^2}{2\alpha_\mathrm{w}}, \frac{k_\mathrm{w}(\Delta y)^2}{2\alpha_\mathrm{w}(1+h_2\Delta y)}\right\} \tag{7}$$

Table 2: Simulation parameters

Parameter	Symbol	Value
Number of nodes	n	41
Wall discretization	Δy	50.0×10^{-6} m

METHOD FOR EXTRACTING UNDERLYING BOUNDARY CONDITIONS

Consider the external wall thermal response $T_{\mathrm{w}1}$ to a step change (in time) in external flow temperature. This is presented in a normalised form—$\phi_{\mathrm{w}1}$ (equation 8)—in figure 3, for the boundary conditions listed in table 3 (typical of lab experiments in which Re is matched, but in which temperature ratio T_{01}/T_{02} is lower than the engine situation). To extract the underlying boundary conditions (h_1 and h_2) from this external wall thermal response, we find the combination of h_1 and h_2 that minimizes the average temperature difference $\overline{|\Delta T_{\mathrm{w}1}|}$ (equation 9) between a particular prediction $T_{\mathrm{w1,ptr}}$ (made using any given combination of h_1 and h_2, and the $T_{01}(t)$ and $T_{02}(t)$ traces associated with the target external wall response) and the target external wall response $T_{\mathrm{w1,trg}}(t)$ (figure 3). The minimization of $\overline{|\Delta T_{\mathrm{w}1}|}$ is performed using the Nelder-Mead algorithm, which is a common derivative-free simplex method to find the arguments minimizing the objective function $\overline{|\Delta T_{\mathrm{w}1}|}(h_1, h_2)$.

$$\phi = \frac{T - T_{02}}{\Delta T_{01}} \tag{8}$$

$$\overline{|\Delta T_{\mathrm{w}1}|} = \sqrt{\frac{1}{(t_\mathrm{e}-t_\mathrm{s})}\int_{t_\mathrm{s}}^{t_\mathrm{e}}\left(T_{\mathrm{w1,trg}} - T_{\mathrm{w1,ptr}}\right)^2 \mathrm{d}t} \tag{9}$$

Table 3: Boundary conditions

Boundary condition	Symbol	Value
External HTC	h_1	3.00×10^3 W m^{-2} K^{-1}
Internal HTC	h_2	6.00×10^3 W m^{-2} K^{-1}
External flow time constant	τ_{step}	0.00 s
Step change amplitude	ΔT_{01}	50.0 K
Internal total temperature	$T_{02}(t)$	298 K

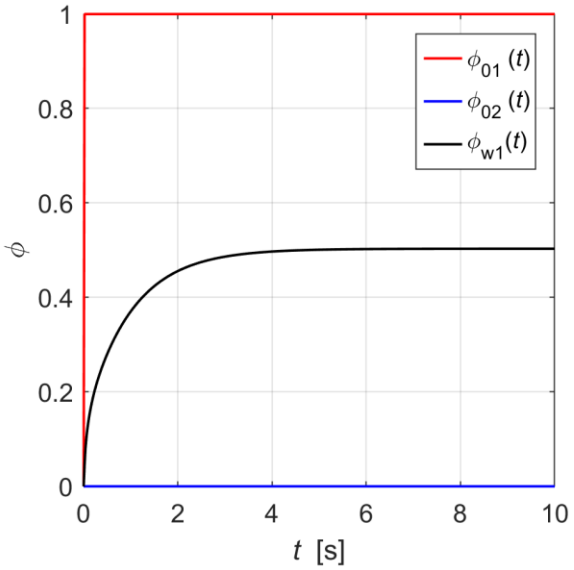

Figure 3: Normalised external wall thermal response to a perfect step change (in time) in external flow temperature

In evaluating the average temperature difference ($\overline{|\Delta T_{w1}|}$) between a particular combination h_1 and h_2, and the target combination h_1 and h_2, a choice must be made about the averaging window (in time) to use, $t_s < t < t_e$. The purpose is to define both the best-fit combination h_1, h_2 and to quantify an increase in error $\overline{|\Delta T_{w1}|}$ as we move away from the best-fit combination. We therefore choose a period $t_s < t < t_e$ which minimises a threshold contour of $\overline{|\Delta T_{w1}|}$ on a map of $\overline{|\Delta T_{w1}|}(h_1, h_2)$. This is done by creating maps of $\overline{|\Delta T_{w1}|}(h_1, h_2)$, for every combination t_s, t_e, and calculating the area enclosed by a threshold contour. The converged values t_s, t_e are insensitive to the particular threshold error that is chosen ($\overline{|\Delta T_{w1}|}$ = 0.5, 1, 2, etc.), provided that it is in the vicinity of the best-fit pair (low absolute threshold). Arbitrarily, a threshold of $\overline{|\Delta T_{w1}|}$ = 1 K was chosen.

The converged values of t_s and t_e are respectively 0.25 s and 6.00 s for a perfect step change in the external flow temperature and the final map of $\overline{|\Delta T_{w1}|}(h_1, h_2)$ for this particular case is shown in figure 4. This time window covers the initial part of the rise (0.25 s < t < 3 s, see figure 3), which is dominated by h_1 and $T_{01}(t)$, up to the approximately steady-state region (3 s < t < 6 s, see figure 3), which is also dependent on h_2 and $T_{02}(t)$. This allows to capture the influence of h_1, h_2, $T_{01}(t)$ and $T_{02}(t)$ in $\overline{|\Delta T_{w1}|}$. The reason why t_s does not equal 0 s is because the initial external wall temperature $T_{w1}(0)$ is always the same for a given $T_{02}(t)$, which doesn't change during this study. Therefore, ΔT_{w1} is always 0 at $T_{w1}(0)$ and hence it is useless to consider it in $\overline{|\Delta T_{w1}|}$. Please note that the values of t_s and t_e are optimized for each external flow time constant.

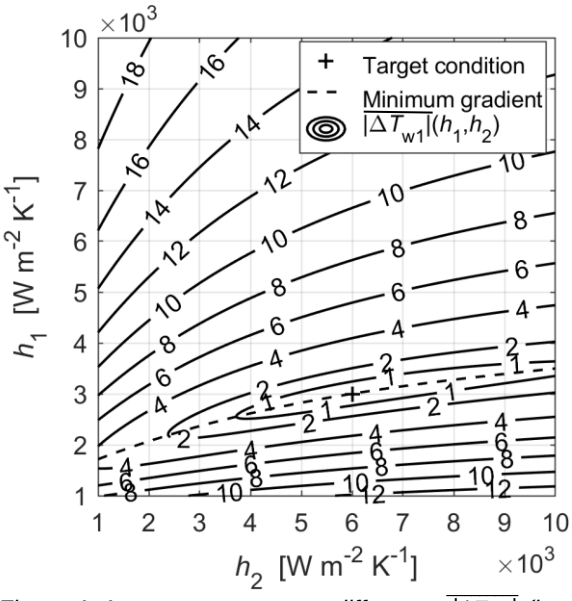

Figure 4: Average temperature difference $\overline{|\Delta T_{w1}|}$ (in K) between wall responses at all combinations h_1, h_2 and the target wall response $T_{w1}(t)$ for a perfect step change in the external flow temperature

When the target temperature trace $T_{w1}(t)$ and input temperature traces $T_{01}(t)$ and $T_{02}(t)$, have no bias or precision errors, then the combination of h_1 and h_2 corresponding to the target external wall response can be extracted without any error. That is, $\overline{|\Delta T_{w1}|}(h_1, h_2) = 0$ for the best-fit pair of h_1, h_2.This is marked by the "+" symbol in figure 4.

The form of figure 4 is interesting. Moving away from the best-fit h_1-h_2 pair (marked by the "+" symbol, the gradient of the error ($\overline{|\Delta T_{w1}|}$) in the h_1 direction is approximately 4 times greater than in the h_2 direction. This is manifested by highly elongated ellipse-like contours on the map of $\overline{|\Delta T_{w1}|}(h_1, h_2)$. Because of the thermal resistance and thermal capacity of the wall, the initial rise (0.25 s < t < 3 s) of $T_{w1}(t)$ is more strongly influenced by h_1 than it is by h_2 (and so far as the dimensional result is concerned, and for the given boundary conditions of temperature step, influenced more by $T_{01}(t)$ than $T_{02}(t)$, but this dependency drops out when results are put in non-dimensional form). The settled value in the quasi-steady-state region (3 s < t < 6 s) is essentially a function of the ratio h_1/h_2, and is therefore equally influenced by both h_1 and h_2. The net result is that when the entire time window is considered (0.25 s < t < 6 s), the error ($\overline{|\Delta T_{w1}|}$) is more strongly influenced by h_1 than by h_2. This is one of the reasons why we have high aspect ratio quasi-elliptical (rather than circular) shape of the solution region for low error ($\overline{|\Delta T_{w1}|}$) thresholds.

IMPACT OF PRECISION AND BIAS ERRORS

In laboratory experiments in which metal effectiveness is measured, there will be a finite measurement uncertainty associated with each of the three temporal responses $T_{w1}(t)$, $T_{01}(t)$ and $T_{02}(t)$. The purpose of this section is to consider the impact of those errors on the accuracy with which boundary conditions h_1 and h_2 can be determined. We do this by considering a distribution of temporal responses $T_{w1}(t)$, $T_{01}(t)$ and $T_{02}(t)$ that have the same mean as those shown in figure 3, but with normally distributed bias and precision errors.

The bias error, β, is introduced by applying a temperature offset to all the temperature traces. The value of the bias error for each temperature trace is randomly picked from a population that is normally distributed with a mean, μ, equal to 0 and a standard deviation, σ, equal to the half of the desired maximum error amplitude, which is expressed as a fraction δ of the external flow temperature step change amplitude ΔT_{01} (e.g. $\sigma = \delta\Delta T_{01}/2$). Thus, 95% of the normally distributed curves lies in a range $T(t) - \delta\Delta T_{01} < T(t) < T(t) + \delta\Delta T_{01}$.

Precision error, ε, is introduced as random white noise of a given amplitude superimposed on the clean signals. The noise amplitude is expressed as a fraction δ of the external flow temperature step change amplitude ΔT_{01} (e.g. $\varepsilon = \delta\Delta T_{01}$).

To quantify the effect of bias and precision errors, underlying target temperature signals are modified with bias and/or precision errors, creating a statistical set of simulated experimental output signals $T_{w1}(t)$, $T_{01}(t)$ and $T_{02}(t)$. These signals are then used with particular combinations h_1 and h_2 to create a statistical set of particular external wall responses, which are compared (in terms of $\overline{|\Delta T_{w1}|}$) to the simulated experimental output external wall responses. This procedure is performed as a Monte Carlo simulation, to determine the distribution of best-fit h_1-h_2 pairs for a given statistical set of simulated experimental output signals. This statistical set of best-fit h_1-h_2 combinations is represented by a 95% confidence region in h_1-h_2 space, for a given simulated experiment (defined by *underlying* signals $T_{w1}(t)$, $T_{01}(t)$ and $T_{02}(t)$ and by bias and precision error ranges, which when combined with the underlying signals give rise to a statistical set of output simulated experimental signals).

We now compute the 95% confidence regions for the output combinations of h_1 and h_2 obtained from Monte Carlo simulations for a number of simulated bias and/or precision errors applied to the input temperature signals. All simulations were for a perfect step change (τ_{step}/τ_{wall} = 0.00) in the external flow temperature. To compute the output error maps (95% confidence regions) 10,000 simulations were performed for each combination of error amplitudes, to represent the statistical distribution of errors around the mean value. The resulting h_1-h_2 pairs are not normally distributed, and therefore the 95% confidence region (in h_1-h_2 space) is not a perfect ellipse. A somewhat arbitrary choice must therefore be made about how to define this region. The high density of output h_1-h_2 pairs allows a definition based on a minimum-area to be used. We calculate the shape of the region containing 95% of the output pairs, which has minimum area, but which is constrained with a limit on the minimum allowable radius of curvature—i.e. the shape must be smooth. The output 95% confidence regions take the form of distorted ellipses. The form of these is justified in the following sections.

The results of this analysis are presented in figures 5 to 7, which deal in turn with: precision error only; bias error only; combined precision and bias error. In all three cases, the area enclosed by the 95% confidence region grows approximately as the fourth power of the error amplitude. Accordingly, because the output (h_1-h_2 pair) 95% error contours are approximately self-similar in shape, across a range of input (precision; bias; or combined precision and bias) error amplitudes, the output error in either h_1 or h_2 grows as approximately the second power of the input error amplitude.

For all three error inputs (precision; bias; or combined precision and bias) we note that h_1 is better constrained than h_2 across the entire range of input error amplitude. Some of the underlying reasons for this have been discussed.

Figure 5 shows results when only a precision error is introduced. The shape of the 95% confidence regions (in h_1-h_2) are similar in form to the contours of constant $\overline{|\Delta T_{w1}|}$ shown in figure 4: highly elongated quasi-elliptical shapes, with greater range in h_2 than in h_1, due to greater sensitivity of the of output $T_{w1}(t)$ signals to h_1 than h_2 during the transient period of the simulation (as opposed to the quasi-steady state period).

Figure 6 shows results when only a bias error is introduced. It is notable that the elongated quasi-elliptical shapes lie along a different major axis to those for the simulations with only precision error (almost perpendicular trends, in fact). Indeed, the individual impact of bias errors on each of the input $T_{01}(t)$, $T_{02}(t)$ or $T_{w1}(t)$ traces, are characteristically different. The impact on each of the three input traces is shown in figure 8.

With reference to figure 8, when a bias error (distribution) is applied to only $T_{01}(t)$, output h_1-h_2 combinations are distributed along the line marked “c” in figure 8. Similarly, when a bias error

is applied to only $T_{02}(t)$, h_1-h_2 solutions lie along line "d". Finally, for bias applied to $T_{w1}(t)$, solutions lie along line "e". The compound effect of normally distributed bias errors (of a given magnitude) applied to all three input temperature trends, is the quasi-elliptical 95% confidence region marked by the solid black line "b". By visualising the three input components (lines of h_1-h_2 solutions, for each of $T_{01}(t)$, $T_{02}(t)$ and $T_{w1}(t)$) we can go some way to checking the final form of the confidence region. Justifying the rotational orientation of this region is more difficult, and requires many individual cases to be examined. Particular cases will be considered in subsequent sections.

When the precision and the bias errors are both applied to the input temperature signals, their effects on the output values of h_1 and h_2 are combined to create a large elliptical confidence region as shown in figure 7. This figure shows well how measurement errors (bias and precision) can lead to large uncertainty in the extracted values of h_1 and h_2. For example, when the precision and bias errors are of ± $0.1\Delta T_{01}$ (black contour on figure 7), h_1 that has a range of 1500 W m^{-2}K^{-1} < h_1 < 4500 W m^{-2} K^{-1} can deviate by up to 1500 W m^{-2} K^{-1} from the target h_1 value, while h_2 that has a range 2500 W m^{-2} K^{-1} < h_2 < 12,500 W m^{-2} K^{-1} can deviate by up to 6500 W m^{-2} K^{-1} from the target h_2.

Figure 9 presents the individual PDFs of h_1 and h_2 at the target condition for the 3 error inputs (precision; bias; and combined precision and bias) of amplitude ± $0.01\Delta T_{01}$. Table 4 lists the 95% confidence intervals of the PDFs shown in figure 9. Each PDF of h_1 was calculated from the h_1-h_2 pairs within the band $h_{2,\mathrm{trg}}$ ± 0.2% for each error type, and vice-versa for the PDFs of h_2. Figure 9 shows that h_1 is well constrained when only precision errors are considered (± 10 W m^{-2} K^{-1} to 95% confidence). When only bias errors with the same distribution are considered, the 95% confidence interval for h_1 is approximately twice the one when only the precision errors are considered. When precision and bias errors are combined, the 95% confidence interval for h_1 grows to more than 11 times the length of the confidence interval when only precision errors are considered. As for h_2, when precision errors, bias errors or combined errors are considered, the 95% confidence intervals are respectively 7, 8 and 43 times longer than the 95% confidence interval for h_1 with only precision errors. For this particular case (perfect step change in the external flow temperature), we see again that h_1 is better constrained than h_2 for a given error type. We also see that the precision errors have a lesser impact on the uncertainty in a given extracted boundary condition than bias errors with the same distribution. When both type of errors are combined, we observe an important increase in the uncertainty of the extracted boundary conditions.

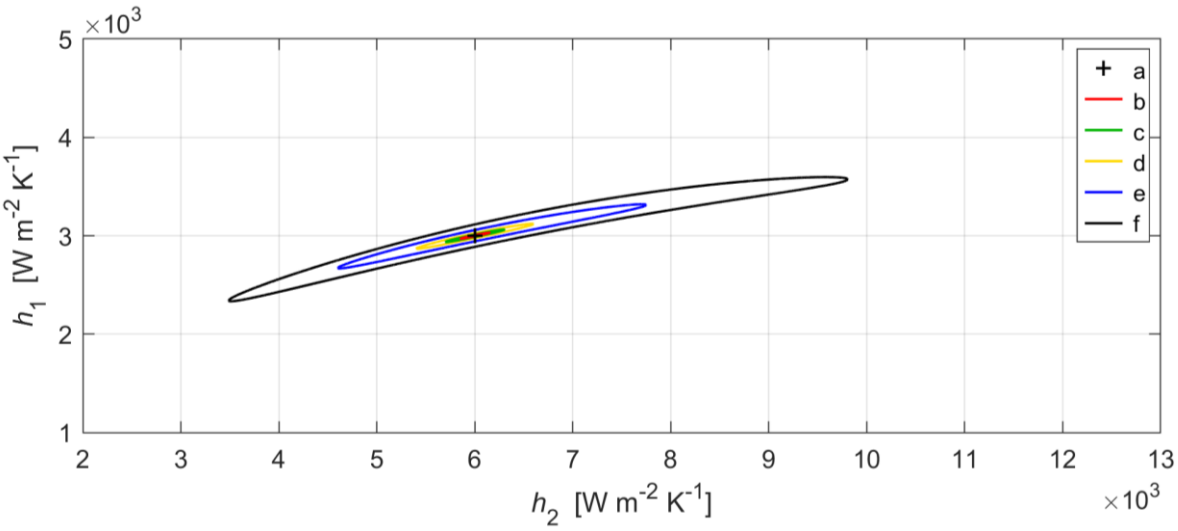

Figure 5: 95% confidence region for extracted h_1 and h_2 combinations for a perfect step change in the external flow temperature (τ_{step}/τ_{wall} = 0.00) with precision errors (ε) defined by: (a) target condition (no error); (b) ε = ± $0.005\Delta T_{01}$; (c) ± $0.01\Delta T_{01}$; (d) ± $0.02\Delta T_{01}$; (e) ± $0.05\Delta T_{01}$; (f) ± $0.1\Delta T_{01}$

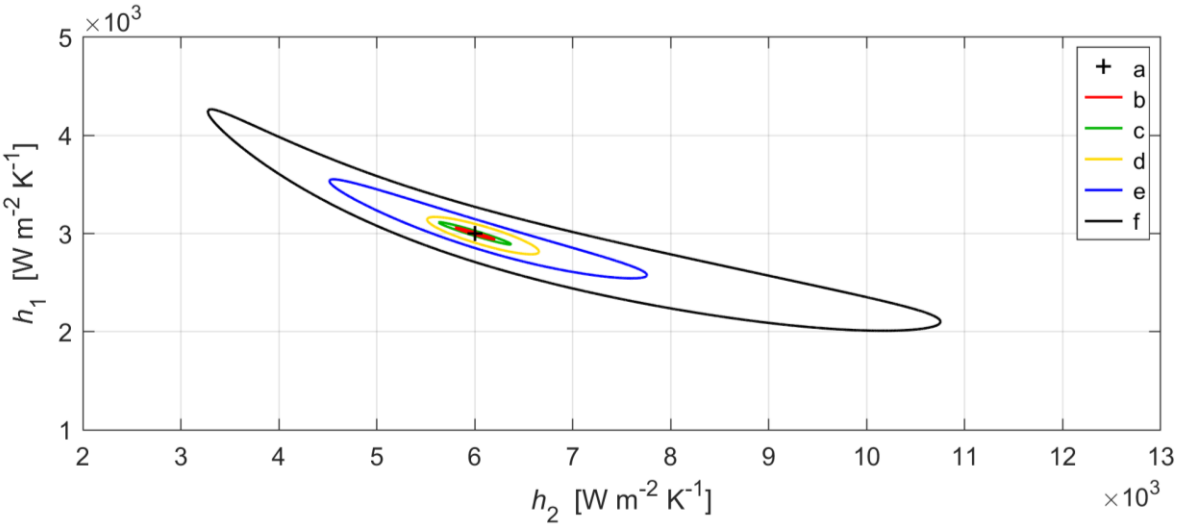

Figure 6: 95% confidence region for extracted h_1 and h_2 combinations for a perfect step change in the external flow temperature (τ_{step}/τ_{wall} = 0.00) with bias errors (β) defined by: (a) target condition (no error); (b) β = ± 0.005ΔT_{01}; (c) ± 0.01ΔT_{01}; (d) ± 0.02ΔT_{01}; (e) ± 0.05ΔT_{01}; (f) ± 0.1ΔT_{01}

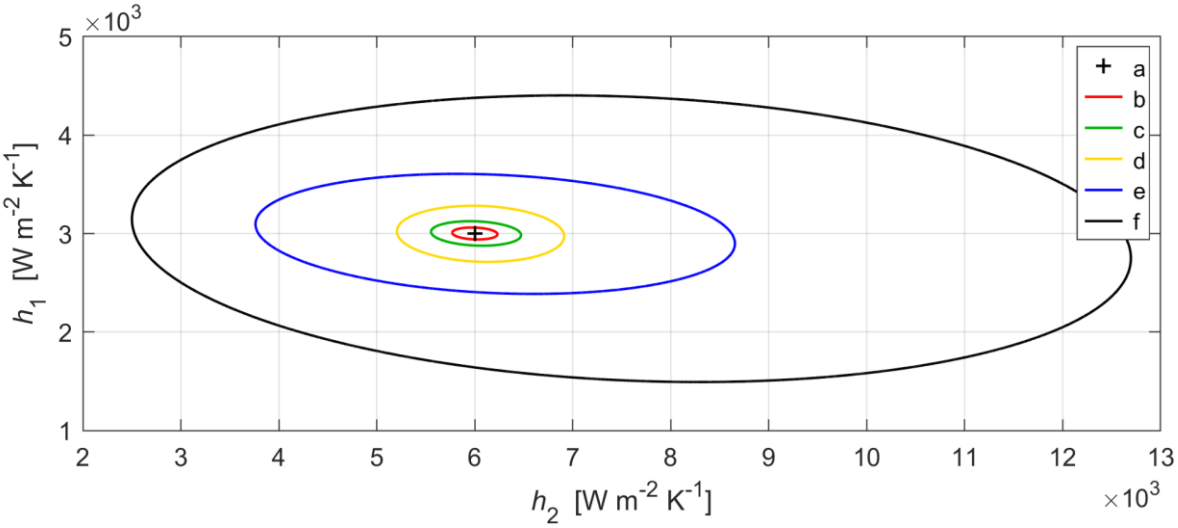

Figure 7: 95% confidence region for extracted h_1 and h_2 combinations for a perfect step change in the external flow temperature (τ_{step}/τ_{wall} = 0.00) with bias and precision errors (β and ε) defined by: (a) target condition (no error); (b) $\beta = \varepsilon$ = ± 0.005ΔT_{01}; (c) ± 0.01ΔT_{01}; (d) ± 0.02ΔT_{01}; (e) ± 0.05ΔT_{01}; (f) ± 0.1ΔT_{01}

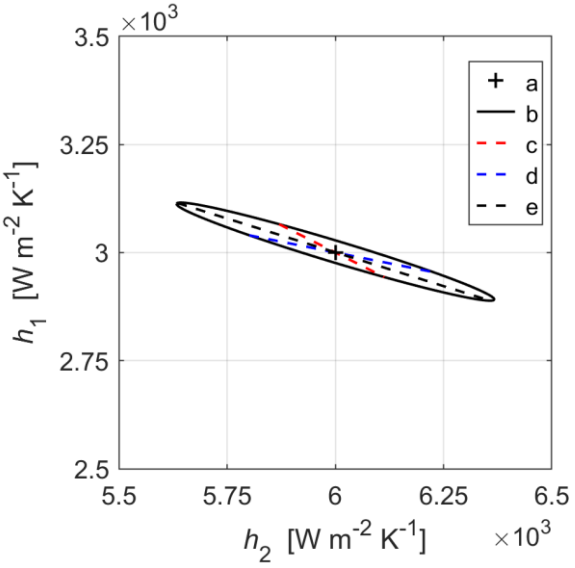

Figure 8: 95% confidence region for h_1 and h_2 for bias errors $\beta = \pm 0.01\Delta T_{01}$ and the line of h_1 and h_1 solutions for each temperature signal: (a) target condition; (b) 95% confidence region; (c) bias error on T_{01}; (d) bias error on T_{02}; (e) bias error on T_{w1}

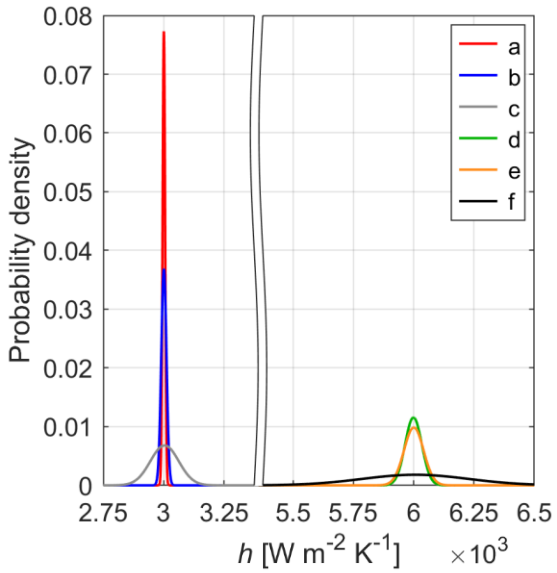

Figure 9: Probability density functions at the target condition: (a) h_1 for $\varepsilon = \pm 0.01\Delta T_{01}$; (b) h_1 for $\beta = \pm 0.01\Delta T_{01}$; (c) h_1 for $\beta = \varepsilon = \pm 0.01\Delta T_{01}$; (d) h_2 for $\varepsilon = \pm 0.01\Delta T_{01}$; (e) h_2 for $\beta = \pm 0.01\Delta T_{01}$; (f) h_2 for $\beta = \varepsilon = \pm 0.01\Delta T_{01}$;

Table 4: 95% confidence intervals of h_1 and h_2 at the target condition for different error inputs

Variable	Input error range, K	95% confidence interval, W m^{-2} K^{-1}
h_1	$\varepsilon = \pm 0.01\Delta T_{01}$	[2991, 3011]
h_1	$\beta = \pm 0.01\Delta T_{01}$	[2982, 3023]
h_1	$\varepsilon = \beta = \pm 0.01\Delta T_{01}$	[2883, 3113]
h_2	$\varepsilon = \pm 0.01\Delta T_{01}$	[5936, 6068]
h_2	$\beta = \pm 0.01\Delta T_{01}$	[5919, 6077]
h_2	$\varepsilon = \beta = \pm 0.01\Delta T_{01}$	[5569, 6439]

IMPACT OF THE TIME CONSTANT OF THE EXTERNAL FLOW TEMPERATURE STEP

To assess the impact of the time constant of the external flow temperature step on the 95% confidence regions for the output values of h_1 and h_2, the procedure to obtain the confidence regions with a perfect step change in external flow temperature is repeated with exponential external flow temperature steps of different time constants τ_{step}. The normalised external flow temperature steps are presented in figure 10, where their respective time constants are normalised by the thermal time constant of the wall. The latter corresponds to the time constant of the best exponential fit of the external wall thermal response to a perfect step change in the external flow temperature as shown in figure 3. The Annular Sector Heat Transfer facility [2] and the Engine Component Aerothermal facility [5], which are two facilities performing overall cooling effectiveness measurements at the University of Oxford, can respectively achieve external flow temperature steps of normalised time constant ($\tau_{\text{step}}/\tau_{\text{wall}}$) of 0.25 and 15.

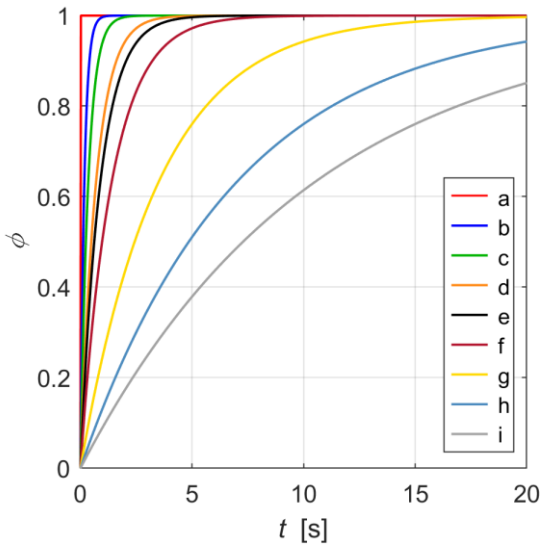

Figure 10: Normalised exponential external flow temperature steps $\phi_{01}(t)$ of various time constants: (a) τ_{step}/τ_{wall} = 0.00; (b) 0.25; (c) 0.50; (d) 1.00; (e) 1.27; (f) 2.00; (g) 5.00; (h) 10.0; (i) 15.0

Figures 11 and 12 respectively present the 95% confidence regions for the output h_1-h_2 pairs for different external flow temperature step time constants. For comparison purposes, we only consider bias errors of $\pm 0.01\Delta T_{01}$ and a combination of bias and precision errors of $\pm 0.01\Delta T_{01}$. The confidence regions as a function of the external flow temperature step time constant with only precision errors considered is not presented since the external flow temperature step time constant has no impact on the confidence region when only a precision error is applied.

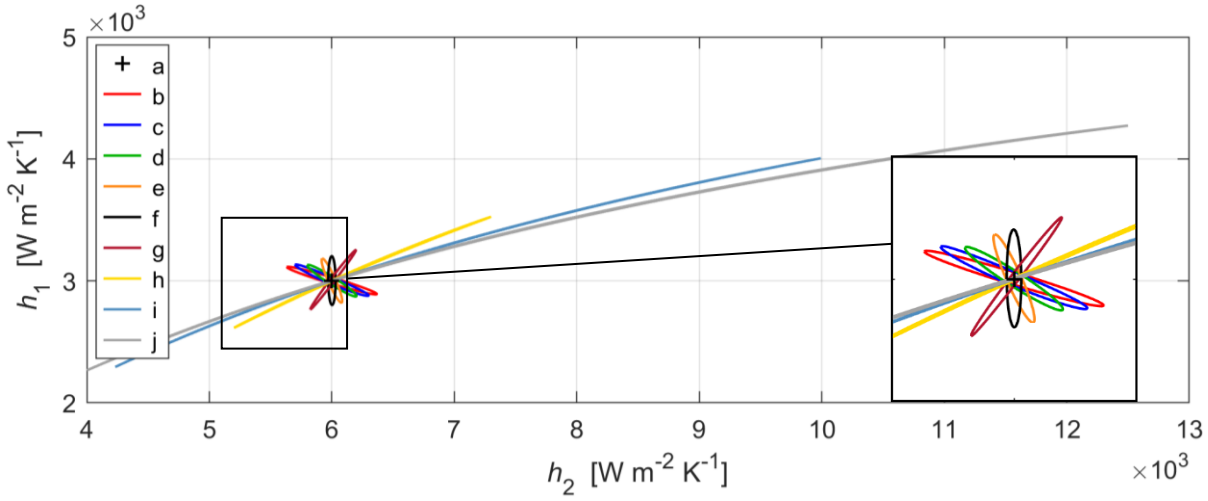

Figure 11: 95% confidence region for h_1 and h_2 combinations as a function of the external flow temperature step time constant for a bias error β = ± 0.01ΔT_{01} : (a) target condition; (b) τ_{step}/τ_{wall} = 0.00; (c) 0.25; (d) 0.50; (e) 1.00; (f) 1.27; (g) 2.00; (h) 5.00; (i) 10.0; (j) 15.0

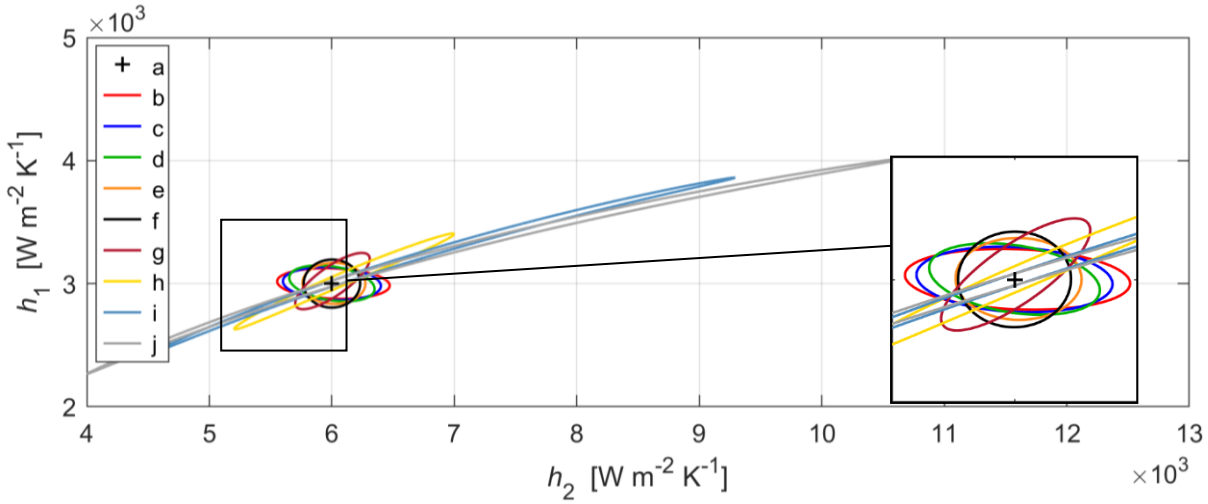

Figure 12: 95% confidence region for h_1 and h_2 combinations as a function of the external flow temperature step time constant for a bias and precision error $\beta = \varepsilon$ = ± 0.01ΔT_{01} : (a) target condition; (b) τ_{step}/τ_{wall} = 0.00; (c) 0.25; (d) 0.50; (e) 1.00; (f) 1.27; (g) 2.00; (h) 5.00; (i) 10.0; (j) 15.0

As presented on both figures 11 and 12, the 95% confidence region for the output values of h_1 and h_2 rotates in the clockwise direction as the external flow temperature step time constant increases. This rotation of the region of h_1 and h_2 solutions is caused by a shift in the required change on h_2 to best-fit the target external wall response with a bias shift as the external flow temperature step time constant increases

To illustrate this, consider figures 13 to 15 which show the normalised true and a positively biased external wall thermal responses (solid and dashed black lines respectively) to external flow temperature steps of different time constants. We can see in figure 13 that when the normalised step time constant ($\tau_{\text{step}}/\tau_{\text{wall}}$) is below 1.27, the external wall thermal response with only an increase in h_1 (orange solid line in figure 13) allows to fit well the rise of the positively biased external wall response but fails to fit the tail of the response. A decrease in h_2 (green solid line in figure 13) is then required to properly fit the tail of the positively biased external wall response. Therefore, when the external flow temperature step is below a normalised value of 1.27, h_1 must be increased and h_2 decreased to best-fit a positively biased external wall response and vice-versa for a negatively biased external wall response. When the external flow temperature step normalised time constant is above 1.27 as shown in figure 15, both h_1 and h_2 must be increased to best-fit a positively biased external wall thermal response and vice-versa for a negatively biased external wall response. When the external flow temperature step normalised time constant is 1.27 as shown in figure 14, only an increase in h_1 is required to fit a positively biased external wall response and vice-

versa for a negatively biased external wall response. Please note that this particular condition where a bias error has no impact on the output value of h_2 is only valid when the bias error is applied only on one of the temperature signals ($T_{01}(t)$, $T_{02}(t)$ or $T_{w1}(t)$) at a specific external flow temperature step time constant and does not occur when bias errors are applied on all 3 signals.

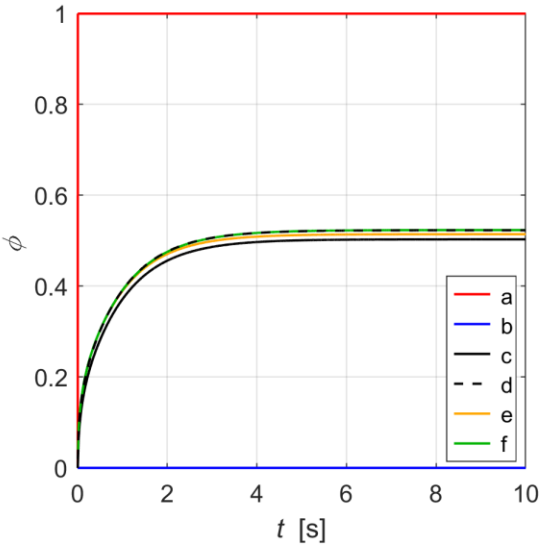

Figure 13: Normalised external wall thermal responses as a function of h_1 and h_2 for τ_{step}/τ_{wall} = 0: (a) $\phi_{01}(t)$; (b) $\phi_{02}(t)$; (c) $\phi_{w1}(t)$, h_1, h_2 = 3.00, 6.00 kW m^{-2} K^{-1}; (d) $\phi_{w1}(t)$ + 0.01, h_1, h_2 = 3.00, 6.00 kW m^{-2} K^{-1}; (e) $\phi_{w1}(t)$, h_1, h_2 = 3.14, 6.00 kW m^{-2} K^{-1}; (f) $\phi_{w1}(t)$, h_1, h_2 = 3.14, 5.58 kW m^{-2} K^{-1}

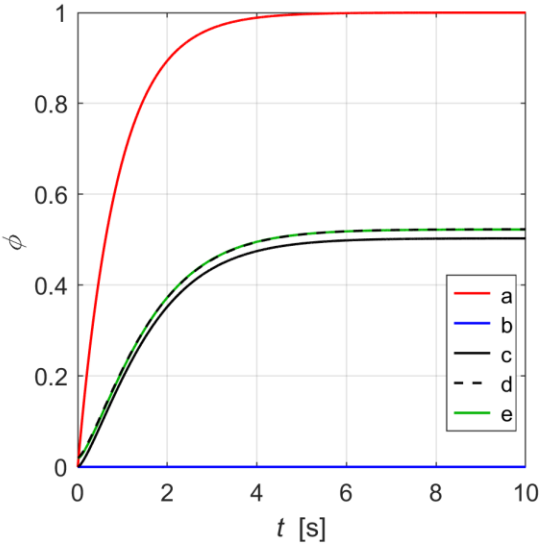

Figure 14: Normalised external wall thermal response as a function of h_1 and h_2 for τ_{step}/τ_{wall} = 1.27: (a) $\phi_{01}(t)$; (b) $\phi_{02}(t)$; (c) $\phi_{w1}(t)$, h_1, h_2 = 3.00, 6.00 kW m^{-2} K^{-1}; (d) $\phi_{w1}(t)$ + 0.01, h_1, h_2 = 3.00, 6.00 kW m^{-2} K^{-1}; (e) $\phi_{w1}(t)$, h_1, h_2 = 3.39, 6.00 kW m^{-2} K^{-1}

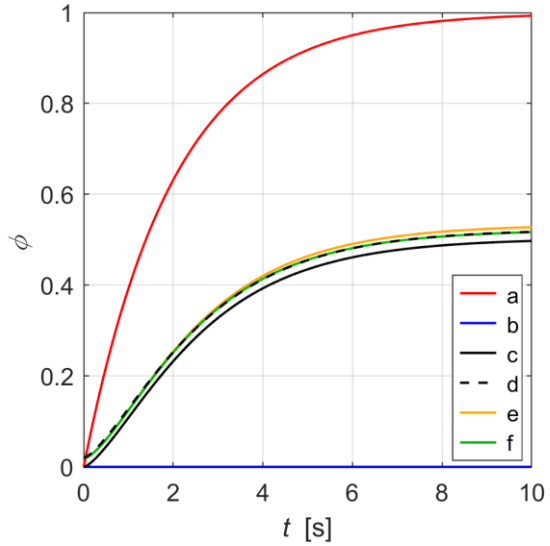

Figure 15: Normalised external wall thermal response as a function of h_1 and h_2 for τ_{step}/τ_{wall} = 2: (a) $\phi_{01}(t)$; (b) $\phi_{02}(t)$; (c) $\phi_{w1}(t)$, h_1, h_2 = 3.00, 6.00 kW m^{-2} K^{-1} (d) $\phi_{w1}(t)$ + 0.01, h_1, h_2 = 3.00, 6.00 kW m^{-2} K^{-1}; (e) $\phi_{w1}(t)$, h_1, h_2 = 3.39, 6.00 kW m^{-2} K^{-1}; (f) $\phi_{w1}(t)$, h_1, h_2 = 3.39, 6.60 kW m^{-2} K^{-1}

Note that when the confidence regions become elongated due to an increasing flow step time constant, particular h_1-h_2 combinations become poorly constrained due to a large 95% confidence region. However, the relationship between the two variables becomes highly constrained due to the elongated and thin shape of the confidence region. This means that if we know one variable (h_1 or h_2) when the external flow temperature step time constant is large ($\tau_{step}/\tau_{wall} \geq 5$), we could determine the other variable more accurately. This will be shown in the next section.

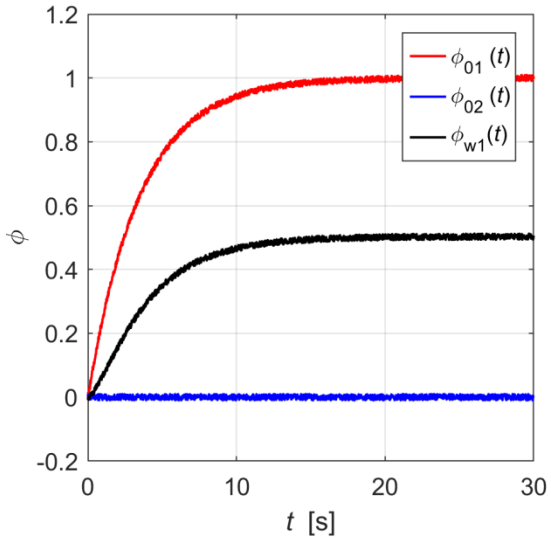

Figure 16: Normalised temperature traces with a bias and precision error $\beta = \varepsilon = \pm 0.01\Delta T_{01}$ with a normalised external flow temperature step time constant τ_{step}/τ_{wall} = 5

PRACTICAL APPLICATIONS

Consider a metal effectiveness experiment in which the transient normalised temperature traces $\phi_{01}(t)$, $\phi_{02}(t)$ and $\phi_{w1}(t)$ are as shown in figure 16.

In this example, the normalised external flow temperature time constant (τ_{step}/τ_{wall}) is 5, and the bias and precision errors are of amplitude ± $0.01\Delta T_{01}$.

The following subsections provide practical examples in which underlying boundary conditions are extracted from transient temperature traces like those in figure 16.

Example 1: both h_1 and h_2 are unknown

If both h_1 and h_2 are unknown, we can obtain a 95% confidence region of possible combinations of h_1 and h_2 (figure 17) that satisfy the measurements $T_{01}(t)$, $T_{02}(t)$ and $T_{w1}(t)$. The most likely combination of h_1 and h_2, and the size of the 95% confidence region (in h_1-h_2 space) depend on both the bias and the precision errors in the measurements of $T_{01}(t)$, $T_{02}(t)$ and $T_{w1}(t)$ and on the time constant of the external flow temperature step.

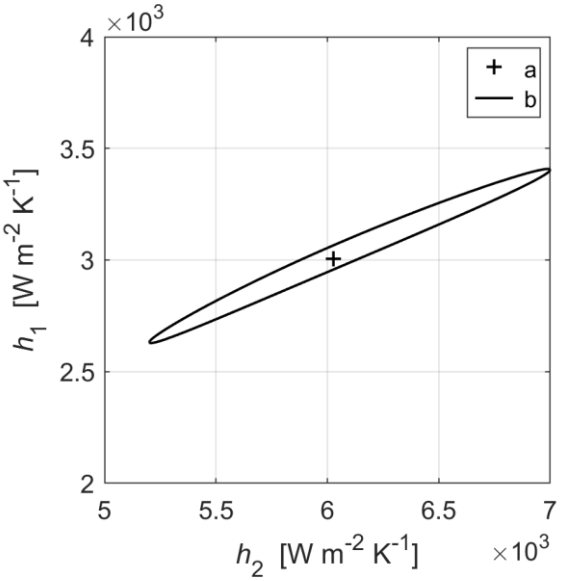

Figure 17: h_1 and h_2 combinations for bias and precision errors $\beta = \varepsilon = \pm 0.01\Delta T_{01}$ and for τ_{step}/τ_{wall} = 5: (a) most likely combination of h_1 and h_2; (b) 95% confidence region for h_1 and h_2.

The most likely output combination of h_1 and h_2 that satisfies the measurements $T_{01}(t)$, $T_{02}(t)$ and $T_{w1}(t)$ is h_1 = 3006 W m^{-2} K^{-1}, h_2 = 6026 W m^{-2} K^{-1}. This is marked by "+" in figure 17. The simulation input values (the underlying values in the numerical experiment) were h_1 = 3000 W m^{-2} K^{-1}, h_2 = 6000 W m^{-2} K^{-1}. As previously mentioned, in a simulation with no measurement uncertainty, the underlying h_1 and h_2 combination would be exactly recovered. Interestingly, the impact of finite measurement uncertainty is not only a statistical distribution of possible h_1 and h_2 pairs (the 95% confidence region in h_1-h_2 space) but also a shift (albeit very small) in the most likely value. That is, we are unable to exactly recover the most likely solution.

Considering the 95% confidence region, we see that for this particular case the range of h_2 (5200 W m^{-2} K^{-1} < h_2 < 7000 W m^{-2} K^{-1}) is more than two times the range of h_1 (2600 W m^{-2} K^{-1} < h_1 < 3400 W m^{-2} K^{-1}). As explained in the previous sections, the external thermal response $T_{w1}(t)$ is more sensitive to changes in h_1 than to changes in h_2 for certain external flow temperature step time constant, which explains the smaller h_1 range. As for the elongated shape of the ellipse, this one comes from the decreasing sensitivity of $T_{w1}(t)$ to changes on h_1 and h_2 at higher step time constant, which requires larger changes on h_1 and h_2 to best-fit the true $T_{w1}(t)$ signal with a bias shift.

Example 2: determination of h_2 when h_1 is known and vice-versa

If h_1 or h_2 is known from another experiment, then it is possible to determine the other parameter by intersecting the measured parameter and its error band with the 95% confidence region obtained from the metal effectiveness experiment to more accurately determine the unknown parameter. For instance, h_1 could be measured to 3000 W m^{-2} K^{-1} (the actual input h_1 value in the simulation) from a very accurate experiment with an error band of ± 2.5% (2925 W m^{-2} K^{-1} < h_1 < 3075 W m^{-2} K^{-1}). In figure 18 the 95% confidence region of figure 17 is intersected with the measured h_1 and its error band. Using the probability density function (PDF) of the measured h_1, we can randomly and normally sample combinations of h_1 and h_2 within the intersection of the 95% confidence region with the error band of the measured h_1. The output PDF of the sampled h_2 provides the confidence we have in h_2. For this particular case, we find that the most likely value of h_2 out of its PDF is 6003 W m^{-2} K^{-1} and its 95% confidence interval is 5801 W m^{-2} K^{-1} < h_2 < 6205 W m^{-2} K^{-1}. The value of h_2 is therefore more accurately extracted than when both h_1 and h_2 are unknown, and the length of its confidence interval is reduced by 4.5 times compared to the confidence interval of h_2 when both h_1 and h_2 are unknown.

The same procedure could be repeated with a known h_2 to determine h_1 with more confidence. For instance, this approach would be of interest when trying to determine the external heat transfer (h_1) of a deteriorated gas turbine vane or blade due to service. If the internal heat transfer coefficient (h_2) is known from the original design since the internal cooling passages do not deteriorate with service, it would be possible to intersect the known

h_2 with the 95% confidence region of possible combinations of h_1 and h_2 obtained from the metal effectiveness experiment performed with the deteriorated parts. This would allow to measure with greater confidence the impact of in-service surface deterioration (oxidation, erosion and deposition) on h_1.

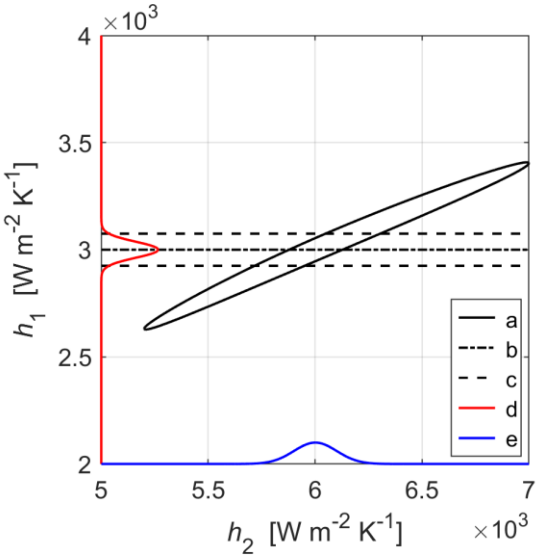

Figure 18: Intersection of the measured h_1 and its error band with the 95% confidence region for h_1 and h_2 when the bias and precision errors are $\beta = \epsilon = \pm 0.01\Delta T_{01}$ and with a normalised external flow temperature step time constant $\tau_{step}/\tau_{wall} = 5$: (a) 95% confidence region; (b) measured value of h_1; (c) uncertainty band on h_1; (d) PDF of measured h_1; (e) PDF of output h_2

Example 3: accuracy with which a design change can be implemented

If the steady state normalised external wall temperature ϕ_{w1} of 0.5 in figure 16 is found to be too high or too low, then a designer might like to take the external wall temperature to another target value $\phi_{w1,trg}$ by changing the heat transfer coefficients.

One simple way to reach $\phi_{w1,trg}$ would be to apply a change on only h_1 (Δh_1) or only on h_2 (Δh_2), which are calculated using equations 10 and 11. The measured point $(h_{1,meas}, h_{2,meas})$ corresponds to the most likely combination of h_1 and h_2 inside the 95% confidence region (marked by "+" in figure 17).

$$\Delta h_1 = h_{1,trg} - h_{1,meas} \quad (10)$$

$$\Delta h_2 = h_{2,trg} - h_{2,meas} \quad (11)$$

To assess the accuracy of the design change (also known as *the extrapolation problem*) we apply a change (Δh_1 or Δh_2) on all the h_1-h_2 combinations within the 95% confidence region. Since Δh_1 and Δh_2 are fixed values and that the true values of h_1 and h_2 can be any combinations inside the confidence region, this means that there will be an uncertainty in the resulting $\phi_{w1,trg}$.

Figure 19 presents the PDF of $\phi_{w1,meas}$ (no HTC change applied) and the PDF of $\phi_{w1,trg}$ depending on its mean value and if it is reached with a change on only h_1 (Δh_1) or only on h_2 (Δh_2) from the measured condition. Table 5 summarises the 95% confidence intervals of $\phi_{w1,meas}$ and all the possible $\phi_{w1,trg}$. Figure 19 shows well that the uncertainty of $\phi_{w1,trg}$ is dependent on its mean value. For instance, the 95% confidence interval of $\phi_{w1,trg} = 0.46$ obtained with Δh_2 is 35% larger than the 95% confidence interval of $\phi_{w1,meas}$. On the other hand, the confidence interval of $\phi_{w1,trg} = 0.54$ obtained with Δh_2 is 62% smaller than the confidence interval of $\phi_{w1,meas}$.

It can also be noticed that the uncertainty in $\phi_{w1,trg}$ is also dependant on the path taken to perform the design change (Δh_1 or Δh_2). For instance, the confidence interval of $\phi_{w1,trg} = 0.54$ obtained with Δh_2 is 38% smaller than the confidence interval of $\phi_{w1,trg} = 0.54$ obtained with Δh_1.

Table 5: 95% confidence intervals on the normalised external wall temperatures

Variable	Mean value	Design change	95% confidence interval
$\phi_{w1,meas}$	0.50	none	[0.4876, 0.5124]
$\phi_{w1,trg}$	0.46	Δh_1	[0.4447, 0.4753]
$\phi_{w1,trg}$	0.46	Δh_2	[0.4432, 0.4768]
$\phi_{w1,trg}$	0.54	Δh_1	[0.5325, 0.5476]
$\phi_{w1,trg}$	0.54	Δh_2	[0.5353, 0.5447]

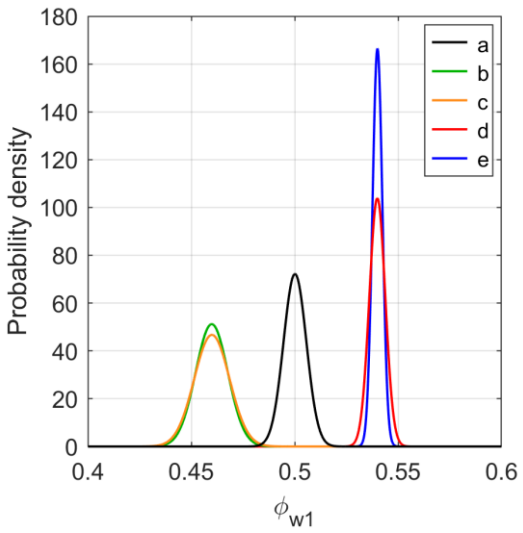

Figure 19: Probability density functions: (a) $\phi_{w1,meas} = 0.5$; (b) $\phi_{w1,trg} = 0.46$ obtained with Δh_1 (c) $\phi_{w1,trg} = 0.46$ obtained with Δh_2; (d) $\phi_{w1,trg} = 0.54$ obtained with Δh_1; (e) $\phi_{w1,trg} = 0.54$ obtained with Δh_2

Figure 19 shows that even though there is a large uncertainty in the extracted values of h_1 and h_2 (large 95% confidence region), it is still possible to accurately achieve design changes, which is the case for $\phi_{w1,trg} = 0.54$ obtained with Δh_2.

Figure 20 allows to understand the dependence of the uncertainty in $\phi_{w1,trg}$ on its value and on the path taken to reach the target condition from the measured point. When a design change (Δh_1 or Δh_2) is applied on the measured condition, we essentially apply a shift on the whole distribution of possible h_1 and h_2 combinations in the h_1-h_2 plane. If the shifted distribution is well aligned with the lines of constant ϕ_{w1}, then $\phi_{w1,trg}$ will be well constrained and vice-versa. For instance, since the shifted distribution of h_1 and h_2 combinations to reach $\phi_{w1,trg} = 0.54$ with Δh_2 is well aligned with the line of constant $\phi_{w1} = 0.54$, there is very little variability in the output distribution of $\phi_{w1,trg}$. On the opposite, the shifted distribution of h_1 and h_2 combinations to reach $\phi_{w1,trg} = 0.46$ with Δh_2 is not well aligned with the line $\phi_{w1} = 0.46$ and goes across other lines of constant ϕ_{w1}. As a result, there is more uncertainty in the output $\phi_{w1,trg}$ for this particular design change.

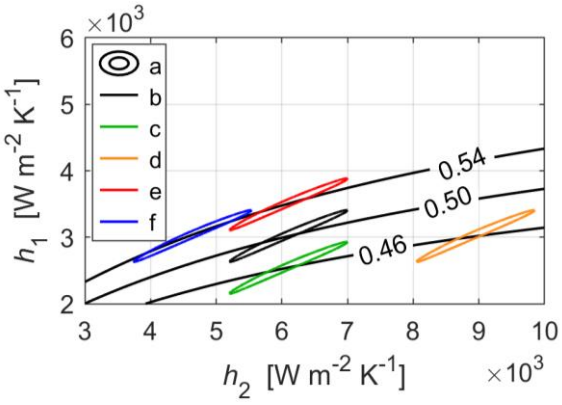

Figure 20: h_1-h_2 map: (a) lines of constant ϕ_{w1}; (b) Measured confidence region for combinations of h_1 and h_2; (c) Shifted confidence region for combinations of h_1 and h_2 to reach $\phi_{w1,trg}$ = 0.46 with Δh_1; (d) $\phi_{w1,trg}$ = 0.46 with Δh_2; (e) $\phi_{w1,trg}$ = 0.54 with Δh_1; (f) $\phi_{w1,trg}$ = 0.54 with Δh_2;

CONCLUSIONS

The purpose of this paper was to present methods to extract the individual underlying boundary conditions from transient metal effectiveness experimental data, and to describe the drivers—in terms, for example, of the precision and bias errors in the directly measured parameters—for the resulting uncertainty in these derived quantities. To explain aspects of this relatively complex problem, we considered the simplest possible system: a one-dimensional heat transfer problem with measured internal and external gas temperatures (with errors), and measured external wall temperature (with errors), and unknown internal and external heat transfer coefficients (the boundary conditions, which were the subject of the study). We showed the following:

i) The uncertainty in the individual underlying values of h_1 and h_2 grows quadratically with the amplitude of the precision and bias errors applied on the three measured temperature signals.

ii) When the time constant of the external flow temperature step is small in comparison to the time constant of the wall ($\tau_{step}/\tau_{wall} \leq 2.00$), possible h_1 and h_2 combinations are tightly constrained (small 95% confidence region in h_1-h_2 space) when measurement errors are low (β, $\varepsilon \leq 0.02\ \Delta T_{01}$).

iii) When the time constant of the external flow temperature step is larger in comparison to the time constant of the wall ($\tau_{step}/\tau_{wall} > 2.00$), possible h_1 and h_2 combinations are relatively poorly constrained even if the measurement errors are low (β, $\varepsilon \leq 0.02\ \Delta T_{01}$).

iv) Interestingly, in some cases (iii) where h_1 and h_2 combinations are relatively poorly constrained, the 95% confidence region can be thin and elongated in h_1-h_2 space. Thus, although the uncertainty associated with picking a *particular* h_1-h_2 pair might be high, the relationship between h_1 and h_2 *within* a pair is relatively low.

v) A consequence of (iv) is that if either h_1 or h_2 is known from another experiment, the remaining parameter can be determined with higher accuracy than if both h_1 or h_2 are unknown.

vi) If a particular metal effectiveness result has been achieved in an experiment, and a design change is required to either increase or decrease the metal effectiveness to a new target value, then for relatively small changes, the new target metal effectiveness can be achieved with an accuracy comparable to the original metal effectiveness result, even in cases where there is significant uncertainty in *individual* underlying parameters h_1, h_2.

Increasing sophistication in metal effectiveness experiments has allowed very detailed assessment of particular cooling system designs. We believe that using analysis of the sort described in this paper —with further developments — it may be possible to go some way to *decoupling* underlying boundary conditions from these experiments, providing deeper insights and understanding of complex coupled systems, making the metal effectiveness technique even more powerful than it currently is.

ACKNOWLEDGMENTS

The support of Rolls-Royce plc is gratefully acknowledged.

REFERENCES

[1] Albert, J. and Bogard, D.; 2013. "Measurements of Adiabatic Film and Overall Cooling Effectiveness on a Turbine Vane Pressure Side With a Trench," ASME Journal of Turbomachinery, 135(5), p. 051007.

[2] Luque, S. and Povey, T.; 2011. "A Novel Technique for Assessing Turbine Cooling System Performance," ASME Journal of Turbomachinery, 133(3), p. 031013.

[3] Luque, S.; Batstone, J.; Gillespie, D.; Povey, T. and Romero, E.; 2013. "Full Thermal Experimental Assessment of a Dendritic Turbine Vane Cooling Scheme," ASME Journal of Turbomachinery, 136(2), p. 021011.

[4] Luque, S.; Jones, T. and Povey T.; 2017. "Effects of Coolant Density, Specific Heat Capacity, and Biot Number on Turbine Vane Cooling Effectiveness," ASME Journal of Turbomachinery, 139(11), p. 111005.

[5] Kirollos, B.; Lubbock, R.; Beard, P.; Goenaga, F.; Rawlinson, A.; Janke, E. and Povey, T.; 2017. "ECAT: An Engine Component AeroThermal Facility at the University of Oxford," ASME Paper No. GT2017-64736, ASME Turbo Expo 2017: "Turbomachinery Technical Conference and Exposition, Charlotte", NC, USA.

[6] Kirollos, B. and Povey T.; 2017. "Laboratory Infrared Thermal Assessment of Laser-Sintered High-Pressure Nozzle Guide Vanes to Derisk Engine Design Programs," ASME Journal of Turbomachinery, 139(4), p. 041009.

[7] Alizadeh, M.; Izadi, A. and Fathi, A.; 2014. "Sensitivity Analysis on Turbine Blade Temperature Distribution Using Conjugate Heat Transfer Simulation," ASME Journal of Turbomachinery, 136(1), p. 011001.

[8] Chowdhury, N.; Zirakzadeh, H.; Han, J. C.; 2017. "A Predictive Model for Preliminary Gas Turbine Blade Cooling Analysis," ASME Journal of Turbomachinery, 139(9), p. 091010.

[9] Takahashi, T.; Watanabe, K.; and Sakai, T.; 2005. "Conjugate Heat Transfer Analysis of a Rotor Blade With Rib-Roughened Internal Cooling Passages," ASME Paper No. GT2005-68227, ASME Turbo Expo 2005: Power for Land, Sea, and Air, Reno, NV, USA.

[10] Zecchi, S.; Arcangeli, L.; Facchini, B. and Coutandin, D.; 2004. "Features of a Cooling System Simulation Tool Used in Industrial Preliminary Design Stage," ASME Paper No. GT2004-53547, ASME Turbo Expo 2004: Power for Land, Sea, and Air, Vienna, Austria.

[11] Special Metals Corporation, 2004. "Inconel® Alloy X-750," Technical report.

[12] Bergman, T., Lavine, S.; Incropera, F. and Dewitt, D.; 2011. "Fundamentals of Heat and Mass Transfer," 7th Edition, John Wiley & Sons, ISBN 13 978-0470-50197-9